

Article

Thermal Impact Analysis and Electric–Thermal Coupled Modeling of Photovoltaic/Battery Space Power System with Different Surface Coatings

Jingyan Xie, Yun-Ze Li ^{*}, Lizhu Yang and Yuehang Sun

School of Aeronautic Science and Engineering, Beihang University, 37 College Rd., Haidian District, Beijing 100191, China

* Correspondence: buaalyz@163.com; Tel.: +86-010-8233-8778; Fax: +86-010-8231-5350

Abstract: Thermal performance has long been recognized as a critical attribute for space systems. Thermal control surface coating is a common method in passive thermal protection. Unfortunately, limited analyzing models and data on the influence of thermal control coatings' α/ε (absorptivity/emissivity) on the space power system have been published to date. To fill this gap, we proposed a multiphysics model that combined environmental temperature calculating and electrical performance analysis together for the satellite power system. In this paper, different coating materials are applied to the radiator surface and thermal insulation surface, respectively. Additionally, a new concept of energy storage, named energy storage voltage, is introduced. The results are analyzed and parametric fits with different formulas using ordinary least squares are conducted. Finally, the change rules are presented, which will prove particularly useful to the space industry, for example, in thermal designs and on-orbit battery studies.

Keywords: satellite power system; thermal control coating; electric–thermal behavior analysis; photovoltaic (PV)/battery space power system; Li-ion battery



Citation: Xie, J.; Li, Y.-Z.; Yang, L.; Sun, Y. Thermal Impact Analysis and Electric–Thermal Coupled Modeling of Photovoltaic/Battery Space Power System with Different Surface Coatings. *Aerospace* **2023**, *10*, 12. <https://doi.org/10.3390/aerospace10010012>

Academic Editor: Xiande Fang

Received: 6 November 2022

Revised: 12 December 2022

Accepted: 21 December 2022

Published: 23 December 2022



Copyright: © 2022 by the authors. Licensee MDPI, Basel, Switzerland. This article is an open access article distributed under the terms and conditions of the Creative Commons Attribution (CC BY) license (<https://creativecommons.org/licenses/by/4.0/>).

1. Introduction

As the space environment is complicated, applied thermal control coatings to spacecraft have become a widespread method of passive thermal protection. Thermal control has long been recognized as a critical attribute for space systems and an essential metric in spacecraft design and optimization. For example, rear-surface mirrors were used on satellites' surfaces to dissipate large amounts of internal heat and provide a low operating temperature [1,2]. Thermal control coatings applied to the space station kept the temperature in acceptable ranges [3]. Changing the emissivity of the solar array surface coating can control the supercooling and overheating of the power generation system [4]. In brief, high flux heat acquisition with tight temperature control is a major requirement in space [5].

To satisfy thermal demands, a lot of new materials were developed as new-type space coatings. Haddad et al. developed a VO₂-based tunable-emittance space coating which allowed a positive switching of the emittance with the temperature [6]. Sydney Taylor et al. simulated a VO₂-based nanophotonic variable-emittance coating in a cold space environment [7]. Their study results showed that this nanophotonic coating could be used for spacecraft thermal control with excellent temperature stability and resistance to thermal cycling. Another thermoregulating material—Li₄Ti₅O₁₂ (LTO) was studied by Jyotirmoy Mandal et al. [8]. LTO could transition from a super-broadband optical reflector to a solar absorber and thermal emitter. LTO also attained a large tunable temperature difference (18 °C) under sunlight, making it a prospective material in space. In addition, Christopher L. Bertagne et al. designed a new radiator concept using shape memory alloy geometry [9]. The thermal-driven deformation effect allowed passive control of the primary surface emissivity.

It is well known that the ratio of absorptivity to emissivity (α/ε) determines a coating's thermal performance [10]. However, how thermal control coating's α/ε affects the thermal environment and internal electrical equipment is still unknown. Amir Hossein Fartash in his research studied the barrier coating system under various types of thermal loadings and found that the transient temperature fields strongly depend on the type of thermal load and thermal properties of the coating [11]. Unfortunately, despite the recognition of its importance, only a small amount of research on the electric–thermal behavior of space power systems has been published to date. Most of the analysis models are, however, focused on explaining the temperature variation in thermal design [12,13] and the coating selections based on transient-state temperature [14]. The electric–thermal behavior, changed due to the α/ε , has not been considered yet.

The Li-ion battery in space is instable, and the power system faces many challenges. Large temperature difference brought by light alternation is a unique challenge to satellite power systems [12]. For example, the surfaces of the International Space Station were subjected to temperature cycles between 173 K and 373 K every 45 min [7]. Some active thermal control technologies were added to the space energy system. Shengnan Wang presented a forced gas cooling strategy combined with a liquid cooling plate for Li-ion batteries in space [15]. The temperature uniformity and the temperature control effectiveness could increase by 2.42 times and 2.61 times more than traditional vacuum packages, respectively. Hui-juan Xu used a single-phase fluid loop that employed active control strategies to adjust the cooling ability of the Li-ion battery pack [16]. Additionally, significant reductions in battery capacity happen in cold conditions [17], which is a problem when the satellite moves into the shadow area. Li-ion batteries are very sensitive to temperature. At low operating temperatures, chemical-reaction activity and charge–transfer velocity will be slow, which leads to a decrease in ionic conductivity in the electrolytes and lithium-ion diffusivity within the electrodes [18]. Considering this bad effect, Mingyun Luo reported a full-temperature thermal management with a composite phase change material [19]. This thermal management of Li-ion batteries could provide a comfortable thermal environment of 20–55 °C under extreme conditions of $-40\sim+50$ °C. Overcharge is another important reason that may cause the failure of the Li-ion batteries [20]. To avoid overcharge and overdischarge, additional battery control units were added to spacecraft. NASA had re-designed the Li-ion Rechargeable Extravehicular Activity Battery Assembly to reduce the risk of a catastrophic thermal runaway incident [21]. This is an important matter because the performance of batteries directly affects the health of satellites. As a result, the performance analysis model of the power system in the satellite is vital. However, research on how the coating's α/ε affects the satellite's inner environment and power system is unclear.

To fill the gap in theoretical studies around α/ε of different coatings, and by the same token observing the electric–thermal behavior of satellite power systems, we conducted a multiphysics model of the satellite power system. The proposed model comprehensively considers the satellite's environment temperature and the electrical performance of the Li-ion battery. In this study, some coating materials are selected to analyze the impacts of different α/ε on the satellite power system and batteries. Our objective is to find the relationship between surfaces' α/ε and the electric–thermal behavior of satellite power systems. In addition to finding the change rules, research data parametric fits are conducted with different formulas using ordinary least squares.

The main contributions of this study are as follows:

- (a) A multiphysics model is introduced to analyze the electric–thermal behavior of space systems. Dynamic temperature models are developed to simulate the thermal environment of the satellite power system, from which the thermal effects of the surface's coating can be observed. In temperature-influenced electrical models, the key electrical parameters of the Li-ion battery pack and single cells are expressed.
- (b) The change rules of temperatures and electric–thermal behavior with coating's α/ε is clear. Error analysis and data fitting are conducted to investigate the accuracy

of regularities. The results presented in this work should prove useful to the space industry, for example, in thermal designs and on-orbit battery studies.

The remainder of this paper is organized as follows. The architecture of the satellite power system, on behalf of the typical space power system and current issues of interdisciplinary performance, is introduced in Section 2. In Section 3, the comprehensive models of the satellite Li-ion battery power system and the simulation procedure are presented. Based on the model of Section 3, parametric analysis and fitting are displayed in Section 4, and the change rules are qualitatively analyzed. Finally, in Section 5, the study results are evaluated and concluded.

2. Architecture of Space Li-Ion Battery Power System and Current Issues of Interdisciplinary Performance

2.1. Architecture of Space Li-Ion Battery Power System

The space power system is formed by solar arrays, storage batteries, power controller and a power regulator module. Due to its long lifetime and high energy density, the Li-ion battery gradually replaced the traditional energy storage battery and became the main strength of the space energy storage component [22]. The architecture of a satellite and its power system are introduced in Figure 1a. To guarantee the thermal status of the battery pack, thermal bus is added, which could transfer heat to the radiator surface.

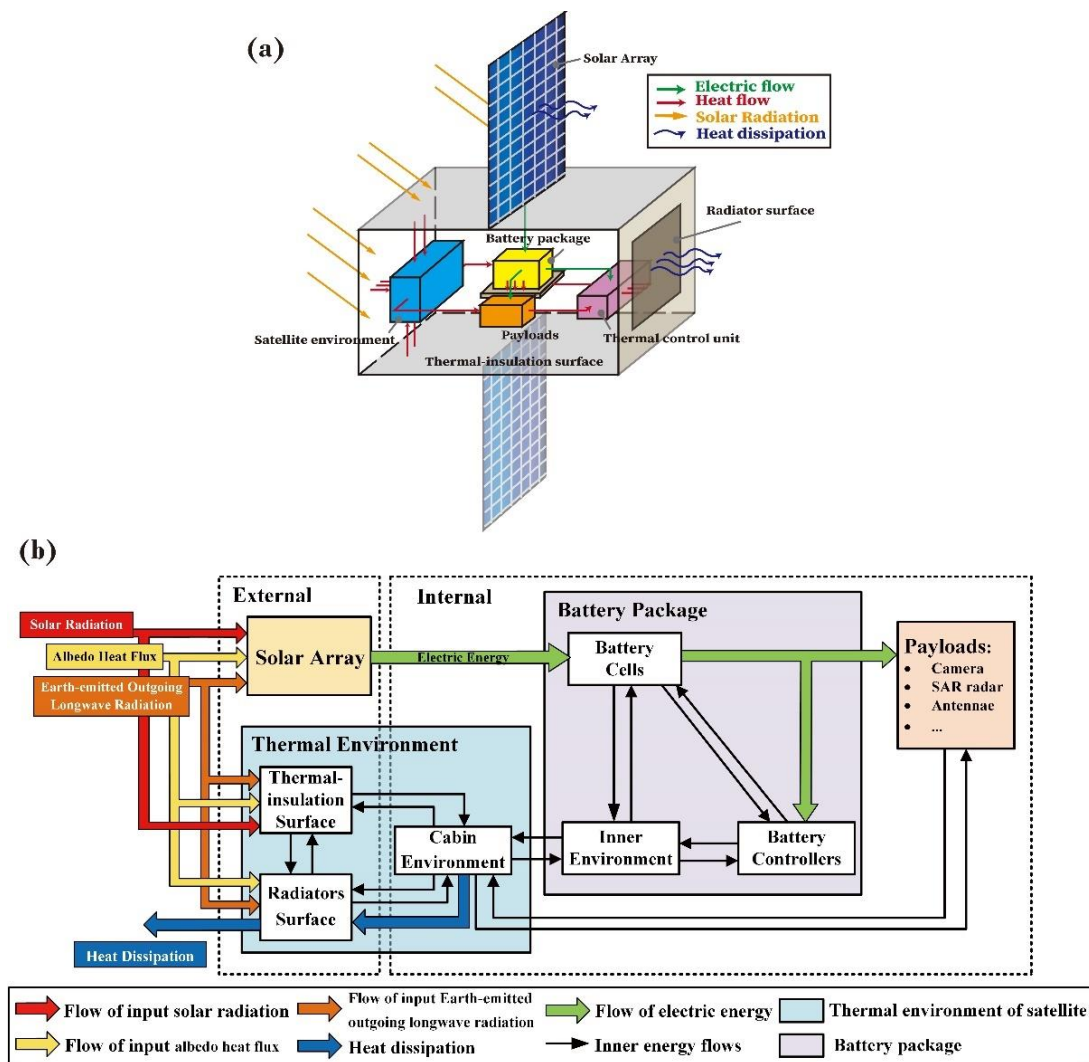


Figure 1. (a) Structure of the satellite and the energy flow; (b) Energy exchange diagram in the satellite.

The energy flows in the satellite power system are shown in Figure 1b. There are two main energy types in the space Li-ion battery system: electrical energy and thermal energy. Electricity ensures regular work and simultaneously generates thermal energy. As for the thermal energy, in addition to the heat generated by the payloads while operating, solar radiation and earth radiation also have thermal impacts on the space Li-ion power system.

2.2. Problems in Analyzing Interdisciplinary Performance and Electric–Thermal Behavior

As described in the previous section, electrical energy and thermal energy are concomitant in the satellite power system. As the space environment is more particular than the ground, the huge temperature difference and complicated conditions make the interdisciplinary performance of the satellite power system difficult to predict. Li-ion batteries' designed operating temperature is 25 °C, and the performance of Li-ion batteries is sensitive to temperature changes. Additionally, the heat generated by inner payloads will conversely affect the thermal condition. Keeping the power system in an acceptable condition is significant. However, the electric–thermal behavior of the satellite power system working in space is unclear. Most of the studies are focused on explaining the low-temperature behavior and the degradation mechanism of the PV/battery power system on the ground. Only a small amount of research has been published which noticed the interdisciplinary performance of satellite power systems.

In addition, thermal control coatings which could change the original thermal radiation characteristics of surfaces are widely used in space passive thermal control. The α/ε has a huge impact on the thermal environment of the satellite. Different thermal control coatings have different α/ε . Studies focused on how α/ε affects the electric–thermal behavior of satellites are fewer.

This research aims to form comprehensive models which could describe the thermal state of the satellite and the electric–thermal behavior of the Li-ion battery in the satellite power system. At the same time, trends in the electric–thermal performance of space power systems with changes of coating will be explored.

3. Comprehensive Models of Satellite Li-Ion Battery Power System

In this section, comprehensive models are developed to analyze the performance of the satellite power system. The models are composed of dynamic temperature models and temperature-influenced electrical models. Calculating formulas of some key performance parameters of Li-ion batteries are given in the temperature-influenced electrical models. Dynamic thermal models describe the thermal environments in the satellite and Li-ion battery pack. Then, in Section 3.3, the parameters of different coatings are represented and their α/ε are given. These selected coatings are used in the thermal insulation surface and thermal dissipation surface of the satellite separately. A designed satellite model is given to simulate the on-orbit performance. The parameters of this designed satellite and its orbit are represented in Table 1.

3.1. Temperature-Influenced Electrical Models

According to the law of conservation of energy, the energy balance equation of a satellite power system is written as Equation (1):

$$P_{sa} + P_B = P_L + P_{un} \quad (1)$$

where P_{sa} is the power output by the solar array; P_B is the power output by the Li-ion battery pack; P_L is the power demand by the payloads; and P_{un} is the unused power. The left side of Equation (1) is the supply side, while the right side is the demand side. As the

demands of a satellite are specific, the charging state of the battery pack is determined by the demands and the power generated by the solar array as shown in Equation (2):

$$\begin{cases} \text{if } P_{sa} \geq P_L \text{ then} \\ \quad \left\{ \begin{array}{l} a = 1 \\ b = 0 \end{array} \right. \\ \text{if } P_{sa} < P_L \text{ then} \\ \quad \left\{ \begin{array}{l} a = 0 \\ b = 1 \end{array} \right. \end{cases} \quad (2)$$

where a and b are state coefficients. When $a = 1$, the battery pack is charging; when $b = 1$, the battery pack is discharging. The temperature-influenced electric models are obtained below.

Table 1. Satellite and orbital parameters.

Parameters	Values
Weight	15 kg
Area of thermal insulation surfaces	2.5 m ²
Area of radiator surface	0.5 m ²
Area of the solar array	2 m ²
Payloads' total power	normal: 120 W; peak: 200 W; peak time: 10 min
Heat efficiency	40%
Orbit altitude	perigee: 170 km; apogee: 400 km
Orbit period	90 min
Shadow period	≈33 min

Solar array

The solar array is the only component that produces energy in a PV/battery power system. The energy harvested from the solar array is shown in Equation (3).

$$P_{sa} = q_1 A_{sa} \alpha_{sa} \eta_{sa} \quad (3)$$

where q_1 is the input solar radiation and η_{sa} is the photoelectric conversion efficiency. In this study, the voltage of the solar array is considered the optimum output voltage $U_{\max_sa} = 30$ V. As the temperature also has an impact on the solar array, the revised voltage is obtained as Equation (4) according to the [23]:

$$U_{sa} = U_{\max_sa} \times (1 - \beta \times (T_{sa} - 298)) \quad (4)$$

where β is the temperature correction coefficient of voltage. From Daniel Tudor Cotfas's study [24], β was between -0.002 and -0.008 depending on the material of the solar cell. In this research, β is set as -0.006 . Additionally, the output current of the solar array is presented in Equation (5):

$$I_{sa} = P_{sa} / U_{sa} \quad (5)$$

Li-ion battery pack

Because of their high energy density and long lifetime, Li-ion batteries are often used as the energy storage battery in satellite power systems. To satisfy the power demands of payloads, many cells are combined in a battery pack. Figure 2 shows the structure of the battery pack. Heat generated in the pack is gathered in the conductive thermal bus, which is associated with the radiator. Beside the pack is the power control unit, which controls the battery's behaviors in the power system. Auxiliary heating patches are also applied to every single cell.

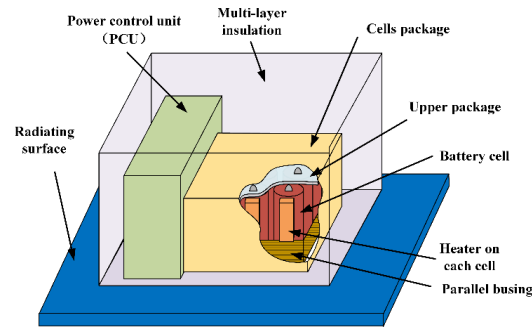


Figure 2. The structure of the satellite battery pack.

As for the single cell, the inner structure is simplified in Figure 3. R_{or} is Ohm resistance; R_{pr} is polarization resistance and R_{dr} is self-discharge resistance. To describe the cell's storage conditions more clearly, energy storage voltage u_d is first introduced in this model. Capacitance C_{E_b} is considered as the power storage module in the simplified model and the voltage across the C_{E_b} is defined as power-storage voltage u_d . As the C_{E_b} and R_d is certain, the state expression of u_d and the energy conservation equation of a cell E_b is shown in Equations (6) and (7). The parameters a and b are on behalf of the states of a single cell. In both dynamic equations, the side with parameter a represents the charging state, while b represents the discharge state.

$$C_{E_b} \frac{du_d}{d\tau} = a \times \left(-\frac{u_d}{R_{dr}} + i_{in} \right) + b \times \left(\frac{u_d}{R_{dr}} + i_{out} \right) \tag{6}$$

$$\frac{dE_b}{dt} = a \times \left(i_{in} \times u_{in} - i_{in}^2 \times (R_{or} + R_{pr}) - \frac{u_d^2}{R_{dr}} \right) - b \times \left(i_{out} \times u_{out} + i_{out}^2 \times (R_{or} + R_{pr}) + \frac{u_d^2}{R_{dr}} \right) \tag{7}$$

where i_{in} and i_{out} represent the charging current and discharging current, respectively. Their expressions are written as Equations (8) and (9):

$$i_{in} = \frac{u_{in} - u_d}{R_{or} + R_{pr}} \tag{8}$$

$$i_{out} = \frac{u_d - u_{out}}{R_{or} + R_{pr}} \tag{9}$$

where u_{in} (Equation (10)) and u_{out} (Equation (11)) are controlled by the voltage outputted by solar array U_{sa} and the voltage demanded by payloads U_L .

$$u_{in} = \frac{1}{n} \times U_{sa} \times \eta_{in} \tag{10}$$

$$u_{out} = \frac{1}{n} \times U_L \times \eta_{out} \tag{11}$$

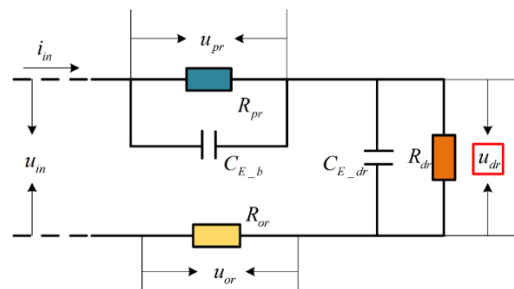


Figure 3. The simplified inner structure model of a single cell.

The SoC can be described as Equation (12):

$$SoC = \frac{\zeta_b}{\zeta_T} = \frac{C_{E-b} u_d}{\zeta_T} \quad (12)$$

where the ζ_T is the actual capacity. ζ_T is determined by the cell's temperature T_b and charge rate I_t . Because there has no specific expression, ζ_T can be expressed as Equation (13):

$$\zeta_T = \zeta_0 \times A_0 \times T_b^{A_1} \times I_t^{A_2} \quad (13)$$

where ζ_0 is nominal capacity and A_0, A_1, A_2 are the fitting parameters. To make the model more comprehensive, the internal resistance $R_{in}(R_a + R_t)$, which is influenced by both cell's temperature T_b and SoC, is shown as Equation (14):

$$R_{in} = (R_{or} + R_{pr}) \times B_0 \times T_b^{B_1} \times SoC^{B_2} \quad (14)$$

The fitting data and the values of these fitting parameters are shown in Appendix A. The reason to establish Equations (13) and (14) is to roughly express the different influence conditions using one equation. On the one hand, the influence of variables such as temperature, charging rate and SoC on the system capacity and state can be observed. On the other hand, the electrical state of the system will also be fed back into the equations, thus reflecting the electric–thermal coupling effect.

3.2. Dynamic Temperature Models of the Space Power System

Satellite thermal environment

According to Figure 1b, solar radiation, albedo heat flux and earth-emitted outgoing longwave radiation are the three main radiation sources for a satellite in low Earth orbit [25]. Additionally, in Figure 1b, a satellite's thermal environment is divided into three parts: thermal-insulation surface, radiator surface and cabin environment. It is considered that temperatures are evenly distributed in these parts. Subscripts c, s, r are defined to represent the cabin environment, thermal-insulation surface with coating and radiator surface separately. Based on the first law of thermodynamics, the average temperature model of three thermal environments is established as Equation (15):

$$C_{H-t} \begin{bmatrix} \frac{dT_c}{dt} \\ \frac{dT_s}{dt} \\ \frac{dT_r}{dt} \end{bmatrix} = K_t \begin{bmatrix} T_c \\ T_s \\ T_r \end{bmatrix} - \begin{bmatrix} 0 \\ \sigma \varepsilon_s A_s T_s^4 \\ \sigma \varepsilon_r A_r T_r^4 \end{bmatrix} + \begin{bmatrix} Q_c \\ Q_s \\ Q_r \end{bmatrix} \quad (15)$$

where Q_c is the sum of the thermal power produced in the cabin environment; Q_s, Q_r are the sum of radiation absorbed by the thermal insulation surface and radiator surface, and the equations are shown in Equations (16) and (17). q is the heat flux and the subscript i represents solar radiation, albedo heat flux and earth-emitted outgoing longwave radiation from 1–3, respectively. The input heat fluxes outside the satellite in this study are shown in Figure 4. As the inner heat flux Q_c shown in Figure 5 is mainly caused by the payloads, the heat efficiency is set at 60%, according to Shengnan Wang's research [15].

$$Q_s = a_s A_s (q_1 + q_2 + q_3) \quad (16)$$

$$Q_r = a_r A_r (q_2 + q_3) \quad (17)$$

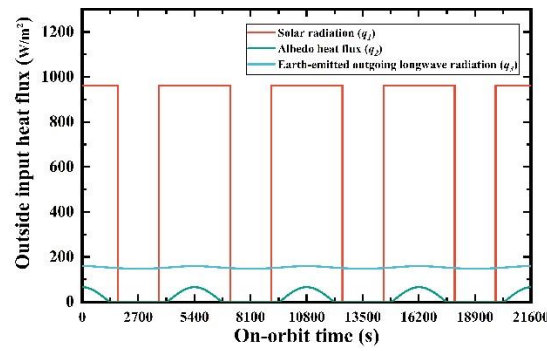


Figure 4. The input heat fluxes outside the satellite.

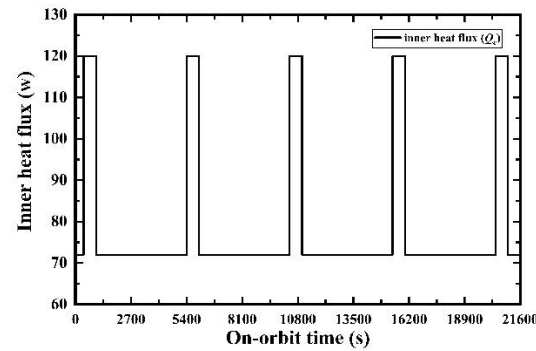


Figure 5. The inner heat flux input in the satellite power system.

C_{H_t} (Equation (18)) is the heat capacity distribution matrix of the thermal environment:

$$C_{H_t} = \begin{bmatrix} C_{H_c} & 0 & 0 \\ 0 & C_{H_s} & 0 \\ 0 & 0 & C_{H_r} \end{bmatrix} \quad (18)$$

K_t is the heat transfer characteristic matrix within the satellite, as Equation (19):

$$K_t = \begin{bmatrix} -(K_{cr}A_{cr} + K_{cs}A_{cs}) & K_{cs}A_{cs} & K_{cr}A_{cr} \\ K_{cs}A_{cs} & -(K_{cs}A_{cs} + K_{sr}A_{sr}) & K_{sr}A_{sr} \\ K_{cr}A_{cr} & K_{sr}A_{sr} & -(K_{cr}A_{cr} + K_{sr}A_{sr}) \end{bmatrix} \quad (19)$$

where k is the overall heat transfer coefficient; subscript cr represents the coefficient between the cabin environment and radiator surface; subscript cs represents the coefficient between the cabin environment and thermal-insulation surface; and subscript sr represents the coefficient between the thermal insulation surface and radiator surface. The specific values are shown in Table 2.

Solar array

Because the solar array in the space power system is not the main research object of this research, the temperature of the solar array is simplified as Equation (20):

$$C_{H_{sa}}m_{sa}\frac{dT_{sa}}{dt} = Q_{sa} - \sigma\varepsilon_{sa}A_{sa}T_{sa}^4 \quad (20)$$

$$Q_{sa} = a_{sa}A_{sa}q_1 \quad (21)$$

where Q_{sa} is the input solar power (in Equation (21)) and subscript sa represents the solar array. The solar array's weight m_{sa} , heat capacity $C_{H_{sa}}$, absorbtivity a_{sa} and emissivity ε_{sa} are reported in Table 2.

Table 2. Thermo-physical properties of the satellite and Li-ion battery cell, and other materials.

	Heat Capacity (J/K)	Heat Transform Coefficient (W/m ² ·K)	Absorptivity	Emissivity	Heat Transfer Area (m ²)
Thermal insulation surface	1300	$k_{cs} = 1.8$	0.8	0.7	2.5
Radiator surface	940	$k_{sr} = 3.5$	0.17	0.88	0.5
Cabin environment	4800	$k_{cr} = 1.43$	-	-	-
Solar array	400	-	0.3	0.5	2
Li-ion cell	80	$k_{bs} = 0.1; k_{bi} = 0.3; k_{br} = 1.98$	-	0.1	$A_{bs}, A_{bi}, A_{br} = 0.007$

Li-ion battery pack

According to the pack structure shown in Figure 6, a single battery cell’s temperature is affected by its surroundings’ temperature, the temperature of the enclosure and the temperature of the radiant surface. When the battery pack does not have an upper package, a battery cell’s temperature is established in Equation (22):

$$C_{H_b} m_b \frac{dT_{b_ij}}{dt} = Q_{b_ij} - k_{bc} A_{bc} (T_{bx} - T_{b_ij}) - k_{br} A_{br} (T_r - T_{b_ij}) - k_{bs} A_{bs} (T_s - T_{b_ij}) + \eta_b Q'_{b_ij} \tag{22}$$

where subscript b_ij is the Li-ion cell in i line j row. Q_{b_ij} is the thermal power produced by cell No. ij ; Q'_{b_ij} is the auxiliary heating power of the No. ij cell and η_b is the efficiency of auxiliary heating. Subscript bc, br, bs mean that the parameter represents the relationship between battery cells and the pack environment, radiator surface, or thermal-insulation surface. T_{bx} is the temperatures in the pack environment and subscript x represents the temperatures in three different zones from 1 to 3.

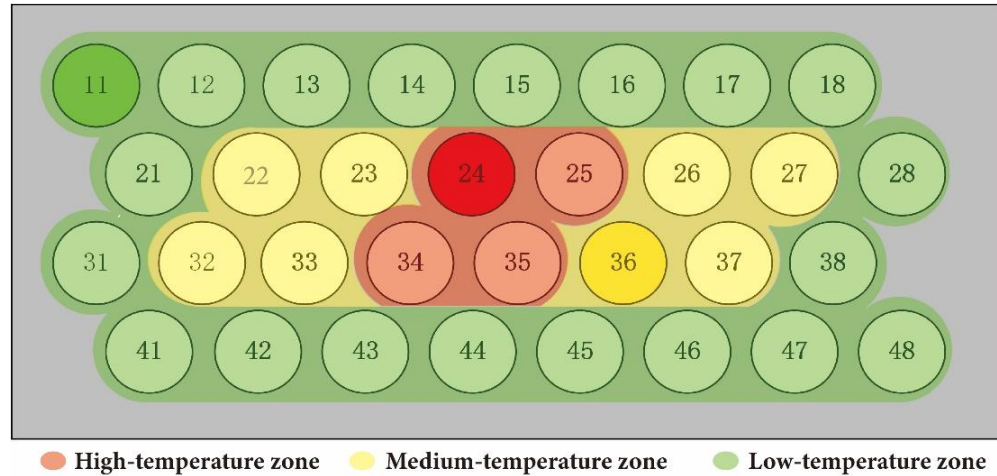


Figure 6. Single cells’ distribution in the battery pack and three zones divided by the temperatures. (Representative batteries No. 11, 24, 36 are in deep colors separately.)

In this model, some assumptions are set: (1) any heat exchange form is inexistent between battery cells; (2) cells’ weight m_b , heat capacity C_{H_b} , thermal efficiency, heat transfer coefficient k_b and heat transfer area A_b are congruous; and (3) the battery pack is divided into three zones according to the temperature distribution shown in Figure 6. The outside cells are defined in the low-temperature zone, as their environment temperature is the lowest, and close to the cabin temperature. The medium-temperature zone comprises cells No. 22, 23, 26, 27, 32, 33, 36, 37. Additionally, cells No. 24, 25, 34, 35 are in the hottest zone in the pack, named the high-temperature zone. The average temperatures of these zones are representative of electric–thermal behavior analysis.

3.3. Selection of Thermal Control Coatings

Though more than one passive thermal control measure must be used in any spacecraft, passive thermal control is the basis of space thermal control. Passive methods rely on the thermal arrangement to adjust the temperature. Thermal control coating is a surface material that can change the surface's radiation properties to achieve thermal control targets. As is well known, the only way for spacecraft to reject heat obtained from inner equipment and space is thermal radiation; coating selection determines the cooling quality of spacecraft.

The thermal-insulation surfaces absorb a lot of radiation in the sunlight zone which is unexpected to enter the cabin. While in the shadow area, the low-temperature environment leads to heat-preserving demand. Hence, the thermal-insulation surfaces need high α/ε coatings [26]. For satellites, the main purpose of the radiator surface is heat dissipation. The coatings used on the radiator surface should have a relatively low α/ε . Some different coatings are selected in this research, and their absorptivity α , emissivity ε and α/ε are demonstrated in Tables 3 and 4.

Table 3. Coating materials for radiator surfaces.

Types	Coatings	Absorptivity α	Emissivity ε	α/ε
Anodizing	Aluminum oxide	0.32	0.74	0.43
	Aluminum alloy	0.3	0.8	0.375
Electroplating	Black nickel plating on aluminum	0.85	0.89	0.96
White paint	S781 white paint	0.17	0.88	0.19
	S956 white paint	0.2	0.85	0.235
	-	0.33	0.73	0.45
	-	0.38	0.73	0.52
Gray paint	S731-SR107	0.69	0.87	0.79
	-	0.45	0.8	0.56
	-	0.55	0.78	0.71
Black nickel plated	Aluminized quartz glass	0.1	0.81	0.12
	Aluminum plating on polyimide film	0.41	0.68	0.6

Table 4. Coating materials for thermal insulation surfaces.

Types	Coatings	Absorptivity α	Emissivity ε	α/ε
White paint	-	0.27	0.86	0.31
Anodizing	Aluminum alloy	0.32	0.74	0.43
Second surface mirror	Polyimide film aluminum plating	0.41	0.68	0.6
Inorganic gray paint	PS17	0.57	0.82	0.7
Gray paint	EZ665ZC	0.72	0.92	0.78
	S956 gray paint	0.78	0.87	0.9
Metallic paint	S781	0.25	0.31	0.81
	ES665NFCG	0.85	0.85	1.0
Black paint	-	0.89	0.88	1.01
	S731-SR107	0.94	0.9	1.04
	S956 black paint	0.93	0.88	1.06
	-	0.8	0.7	1.14
Black nickel plated	Black nickel plating on aluminum	0.85	0.89	0.96
	Black nickel plating on stainless steel	0.92	0.86	1.07

4. Results and Discussions

In this section, thermal and electric analyses are carried out. Three cells (11, 24, 36) belonging to the three zones indicated in Figure 6 are selected to show the research results.

4.1. The Cyclical Effect of α_r/ϵ on Thermal Performance

Radiator surfaces

The radiator surface’s thermal performance affects the thermal control directly. After simulation, the average temperature in the battery pack rises from 279 K to 297 K with the increase of α_r/ϵ . In Figure 7a, the best average temperature for the whole pack is between 0.5 to 0.8 in this simulation. When $\alpha_r/\epsilon < 0.5$, there is a dramatic increase in the average temperature. This proved that when in the low α_r/ϵ range, the rise of α_r/ϵ has a greater impact on the average temperature of the Li-ion battery pack.

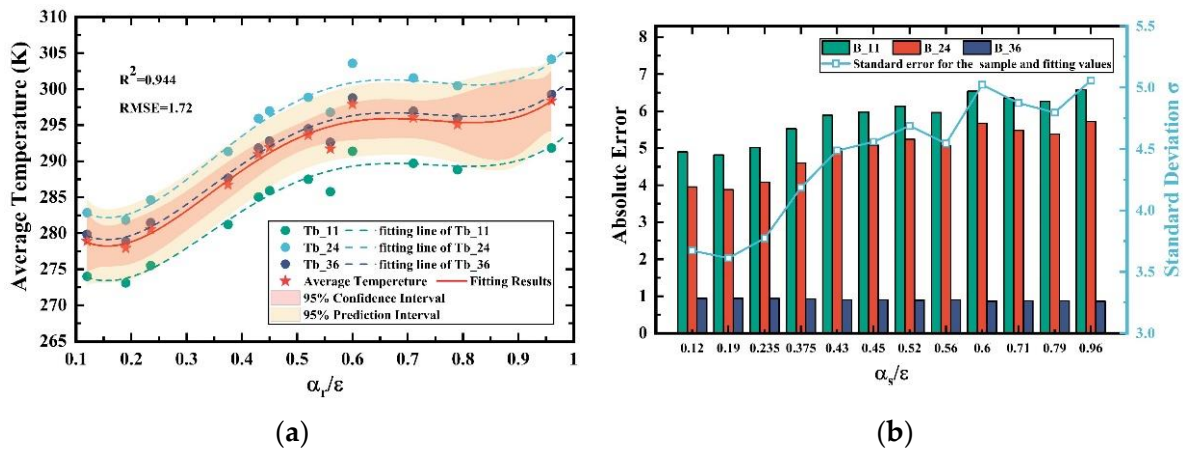


Figure 7. The average temperatures of the battery pack and fitting results with different radiator surface’s coatings: (a) The average temperature changing with α_r/ϵ ; (b) Absolute difference and standard deviation of the single cells’ temperature and the fitting value.

For single cells in Figure 7a, No. 36’s average temperature is closest to the fitting results. Its data points almost fall in the 95% confidence interval of the average temperature fitting line. Some data points of No. 11 and 24 are also in the 95% prediction interval in Figure 7a, and the fitting lines’ parameters are shown in Table 5. The discrete degree of 3 zones’ average temperature climbs with the increasing of α_r/ϵ in Figure 7b should also be noted. When the α_r/ϵ of the radiator surface rises, the temperature difference in the pack would increase, which should be avoided.

Table 5. The fitting polynomial and parameters of average temperatures changing with α_r/ϵ .

Fitting polynomial	$T_{r_i} = a_i + b_i \times \frac{\alpha_r}{\epsilon_r} + d_i \times \frac{\alpha_r^2}{\epsilon_r} + f_i \times \frac{\alpha_r^3}{\epsilon_r} + g_i \times \frac{\alpha_r^4}{\epsilon_r} + h_i \times \frac{\alpha_r^5}{\epsilon_r}$					
Parameters	a_i	b_i	d_i	f_i	g_i	h_i
Whole pack	290.6	−184.72	864.28	−1326	770.18	−113.36
B_11	284.9	−171.9	808	−1255	749.7	−121.2
B_24	295.4	−197.3	918.8	−1390	780.8	−101
B_36	291.5	−184.9	866	−1333	780.1	−117.9
Error analysis	Whole pack	B_11	B_24	B_36		
R-square	0.944	0.945	0.943	0.944		
RMSE	1.72	1.57	1.89	1.72		

The single cells' temperature differences are represented in Figure 8a and the fitting lines' parameters are shown in Table 6. The temperature difference of the battery decreases with α_r/ε rising. The decline of standard deviation between the fitting result and simulating data in Figure 8b declares that the temperature differences of cells become closer. This phenomenon indicates that the cell's peak temperature drops and the temperature fluctuation reduces. A moderate temperature is good for Li-ion cells. These observations are not conflicting with the conclusions obtained from Figure 7. Decreases in the temperature difference of cells do not affect the increasing trends of the average temperature in the battery pack. Though higher α_r/ε benefits single cells, the pack's thermal performance is aforementioned and the α_r/ε of the radiator surface should be relatively lower.

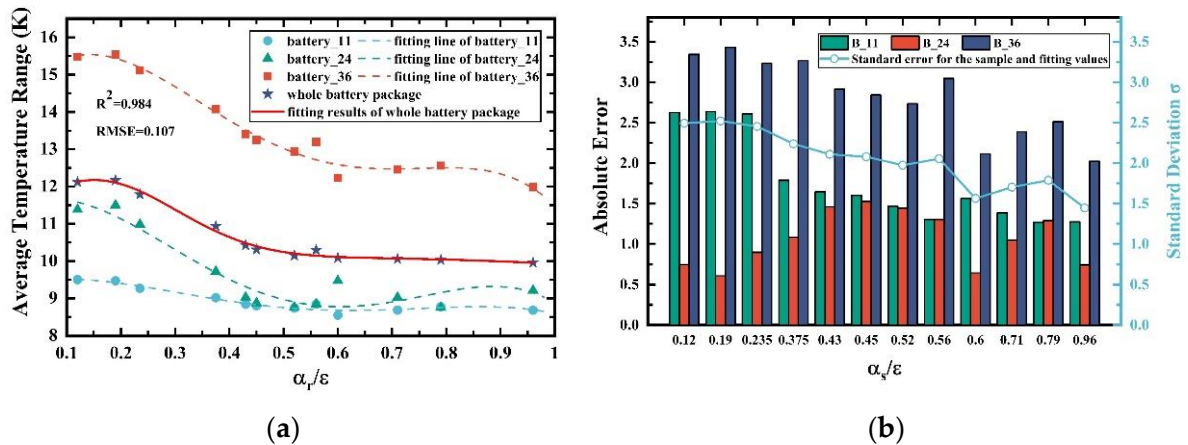


Figure 8. The average temperature differences of the battery pack and fitting results with different radiator surface's coatings: (a) The average temperature differences changing with α_r/ε ; (b) Absolute difference and standard deviation of the single cells' temperature differences and the fitting value.

Table 6. The fitting polynomial and parameters of average temperature differences changing with α_r/ε .

Fitting polynomial 1	$\Delta T_{r_i} = a_i \times \exp(-((\frac{\alpha_r}{\varepsilon_r} - b_i)/d_i)^2) + f_i \times \exp(-((\frac{\alpha_r}{\varepsilon_r} - g_i)/h_i)^2)$					
Parameters	a_i	b_i	d_i	f_i	g_i	h_i
Whole pack	2.28	0.14	0.22	10.08	0.6	3.29
Fitting polynomial 2	$\Delta T_{r_i} = a_i + b_i \times \frac{\alpha_r}{\varepsilon_r} + d_i \times \frac{\alpha_r^2}{\varepsilon_r^2} + f_i \times \frac{\alpha_r^3}{\varepsilon_r^3} + g_i \times \frac{\alpha_r^4}{\varepsilon_r^4}$					
Parameters	a_i	b_i	d_i	f_i	g_i	
B_11	9.357	3.606	-23.42	36.16	-17.11	
B_24	11.32	9.165	-71.08	113.9	-54.43	
B_36	14.11	22.67	-109.2	154.1	-70.2	
Error analysis	Whole pack	B_11	B_24	B_36		
R-square	0.984	0.92	0.96	0.96		
RMSE	0.107	0.09	0.21	0.261		

Thermal-insulation surfaces

In this part, cells No. 11, 24 and 36 are chosen to represent different temperature zones. The average temperatures changing with α_s/ε are shown in Figure 9a. The pack's average temperature climbs from 271 K to 283 K. In Figure 9a, the average temperatures of the chosen cells also grow with the increase of α_s/ε . Though the cells' temperatures in this simulation may be lower, the Li-ion battery pack would have higher performance when $\alpha_s/\varepsilon > 1$.

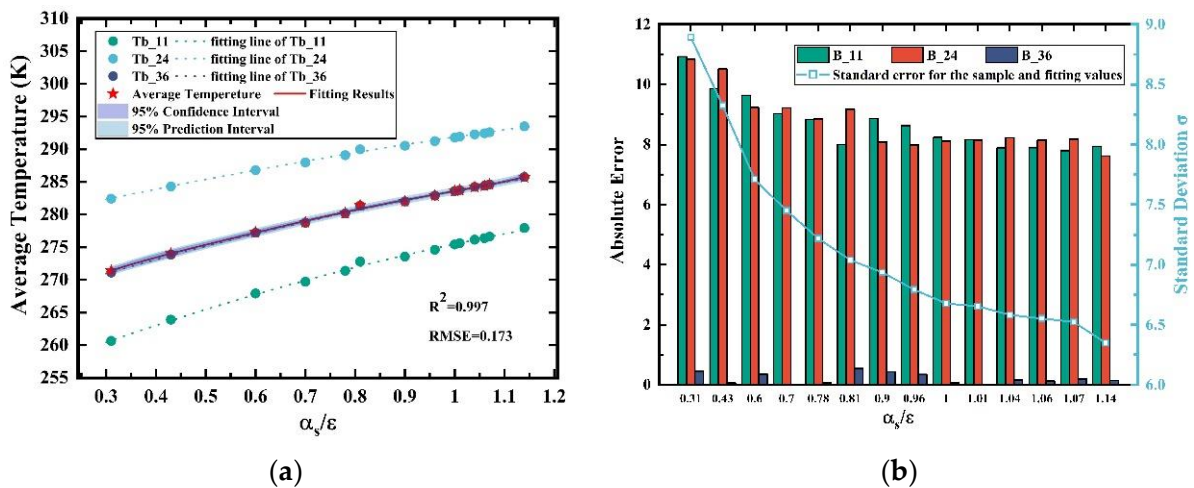


Figure 9. The average temperatures of the battery pack and fitting results with different thermal-insulation surface’s coatings: (a) The average temperature changing with α_s/ϵ in the battery pack; (b) Absolute difference and standard deviation of the single cells’ temperature and the fitting value.

With the statistical analysis of these data, the fitting results are proved in Figure 9a. The least squares method is used in polynomial fittings, and the fitting parameters in different expressions are obtained in Table 7. A 95% confidence interval and a 95% prediction interval of the battery pack’s average temperature are given in Figure 9a. The data points of cell No. 36 are all in the 95% prediction interval, which means that the medium-zone average temperature trend could indicate the pack’s average temperature trend.

Table 7. The fitting polynomial and parameters of average temperatures changing with α_s/ϵ .

Fitting polynomial	$T_{s_i} = a_i + b_i \times \frac{\alpha_r}{\epsilon_r} + d_i \times \frac{a_r^2}{\epsilon_r^2} + f_i \times \frac{a_r^3}{\epsilon_r^3} + g_i \times \frac{a_r^4}{\epsilon_r^4} + h_i \times \frac{a_r^5}{\epsilon_r^5}$					
Parameters	a_i	b_i	d_i	f_i	g_i	h_i
Whole pack	254.95	103.38	−256.84	385.65	−284.59	81.05
B_11	251.9	30.7	−7.12			
B_24	277.3	17.73	−3.154			
B_36	263.8	25.58	−5.75			
Error analysis	Whole pack	B_11	B_24	B_36		
R-square	0.997	0.997	0.998	0.997		
RMSE	0.173	0.265	0.164	0.22		

Figure 9b shows the absolute errors between the cells’ average temperature and the pack’s average temperature. In Figure 9b, the conclusion gained from Figure 9a is proved again: that the average temperature curve of No. 36 can predict the average temperature of the battery pack. Furthermore, the standard deviation has a slump of 6.3 when $\alpha_s/\epsilon = 1.14$. The decline of standard deviation means that the gaps among different temperature zones reduce with the growth of α_s/ϵ .

Figure 10 provides the results and statistical analyses of the temperature differences during the simulation time. The temperature difference is the difference between the maximum temperature and minimum temperature, which reflects the temperature uniformity in the battery pack. The temperature difference decreases with the increase of α_s/ϵ . Single cells’ temperature differences have similar trends. Therefore, improving the α_s/ϵ of thermal-insulation surfaces can reduce the temperature difference in the pack. Cells’ fitting parameters are shown in Table 8.

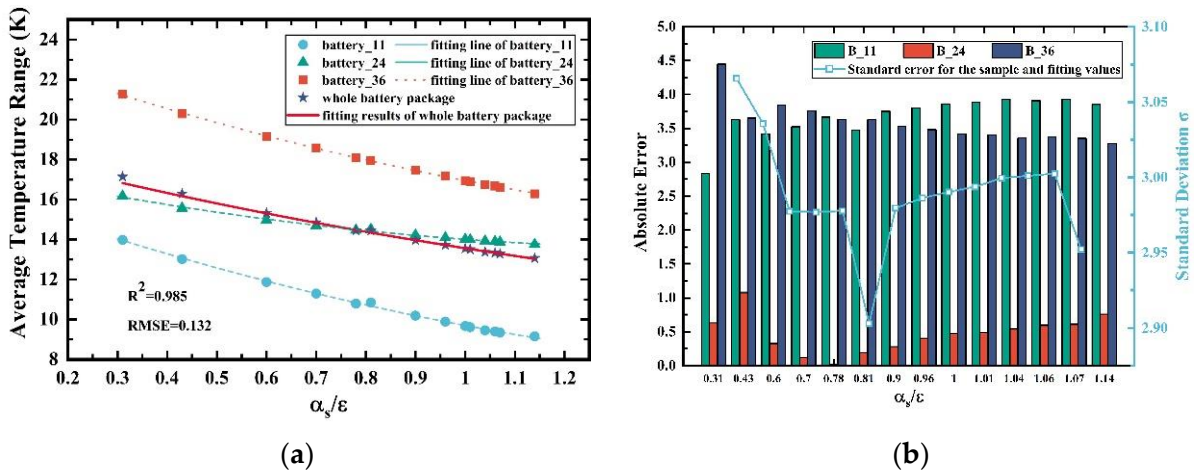


Figure 10. The average temperatures of the battery pack and fitting results with different thermal-insulation surface coatings: (a) The average temperature differences changing with α_s/ϵ ; (b) Absolute difference and standard deviation of the single cells’ temperature difference and the fitting value.

Table 8. The fitting polynomial and parameters of average temperature differences changing with α_s/ϵ .

Fitting polynomial 1	$\Delta T_{s-j} = a_i + b_i \times \exp(d_i \times \frac{\alpha_r}{\epsilon_r})$			
Parameters	a_i	b_i	d_i	
Whole pack	6.11	12.62	−0.53	
Fitting polynomial 2	$\Delta T_{s-j} = a_i \times \frac{\alpha_r}{\epsilon_r}^2 + b_i \times \frac{\alpha_r}{\epsilon_r} + d_i$			
Parameters	a_i	b_i	d_i	
B_11	2.11	−8.93	16.52	
B_24	1.81	−5.43	17.63	
B_36	2.04	−8.86	23.77	
Error analysis	Whole pack	B_11	B_24	B_36
R-square	0.985	0.998	0.996	0.999
RMSE	0.132	0.07	0.046	0.031

For a single cell, the temperature difference in the medium-temperature zone is the highest. The rise of α_s/ϵ has the greatest impact in the low-temperature zone, as the temperature difference of No. 11 decreased by 35% in Figure 10a. The standard deviation in Figure 10b indicates that the difference between the simulation data point and fitting results is nearly unchanged with α_s/ϵ .

4.2. The Cyclical Effect of α/ϵ on Electric–Thermal Coupling Behavior

Radiator surfaces

Figure 11a shows the trend that energy storage voltage changes with α_r/ϵ , and the fitting results are provided in Appendix B (Tables A3–A6). Different fitting methods are applied to the data and the trends are the same: the energy storage voltage of a single cell increases with the rise of α_r/ϵ . As the energy storage voltage is used to indicate the electric quantity of battery storage, its change trend is similar to the trend of maximum capacity shown in Figure 11b. With α_r/ϵ growing, energy storage status improves. The reason for this phenomenon is that the pack’s average temperature rises.

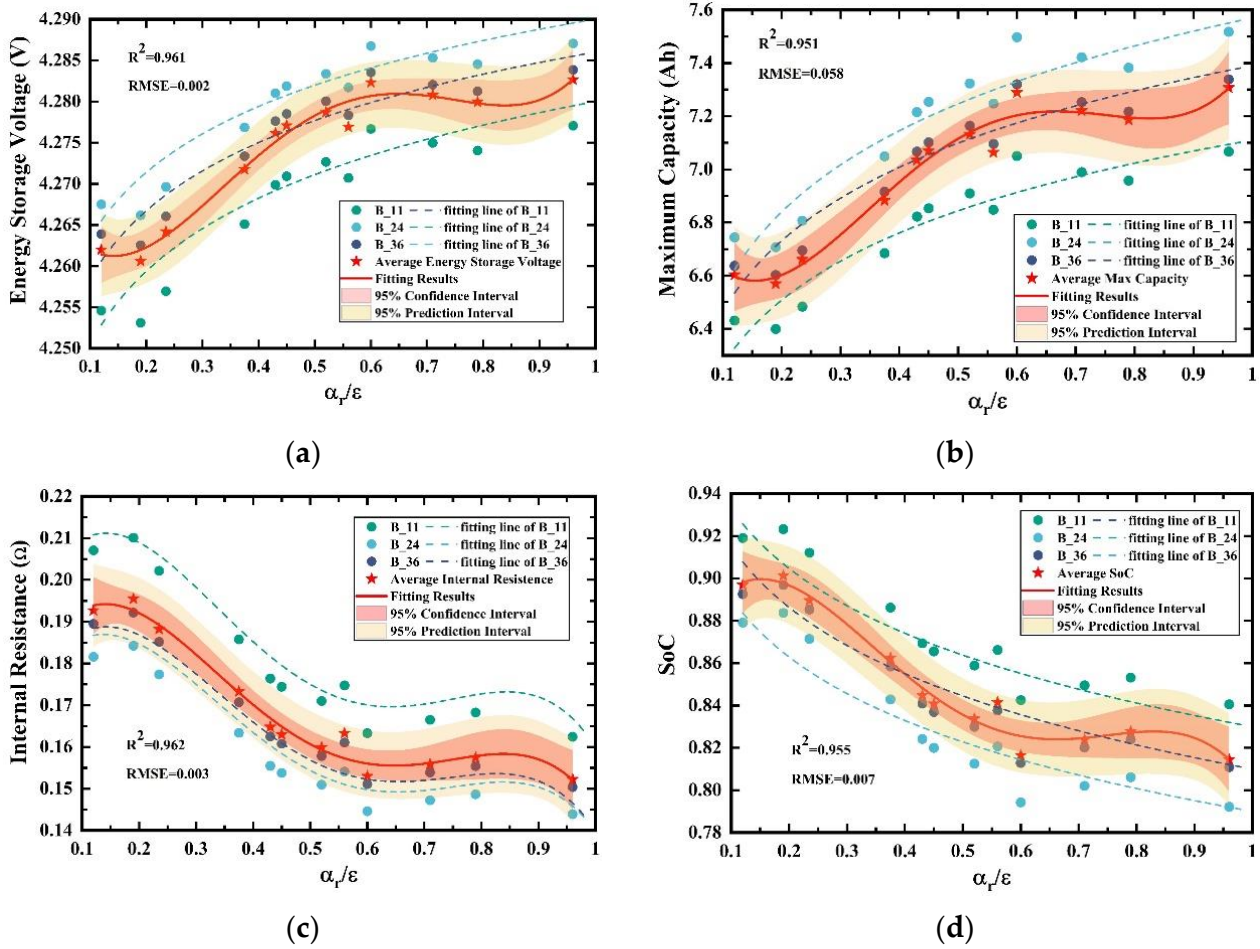


Figure 11. The electric parameters changing with different radiator surface’s coating: (a) energy storage voltage; (b) maximum capacity; (c) internal resistance; (d) SoC.

The internal resistance drops markedly when α_r/ϵ is between 0.2 to 0.6. Lower internal resistance means less internal battery pack consumption and higher efficiency. This is also related to the rising temperature. The results are shown in Figure 11a–c. It seems that a higher α_r/ϵ of radiator surface is better. In contrast, the SoC of the battery pack declines in Figure 11d, which is connected to the increasing maximum capacity. High pack temperature makes the depth of discharge (DOD) grow. When the DoD is above 25%, the aging rate of the battery is accelerated. From this aspect, $\alpha_r/\epsilon > 0.6$ has disadvantages for electric–thermal behavior.

Thermal-insulation surfaces

The thermal-insulation surface’s electric–thermal behaviors changing with α_s/ϵ is shown in Figure 12. Energy storage voltage and maximum capacity increase with α_s/ϵ rising while internal resistance and SoC fall. Change rules are the same for radiator surface, and the fitting parameters are represented in Appendix B (Tables A7–A10).

In a word, the electric–thermal behavior changes with the satellite surface’s α/ϵ , which is independent of the position of surfaces. All the electrical impacts are caused by the temperature. Thus, thermal control is vital for on-orbit satellite power systems.

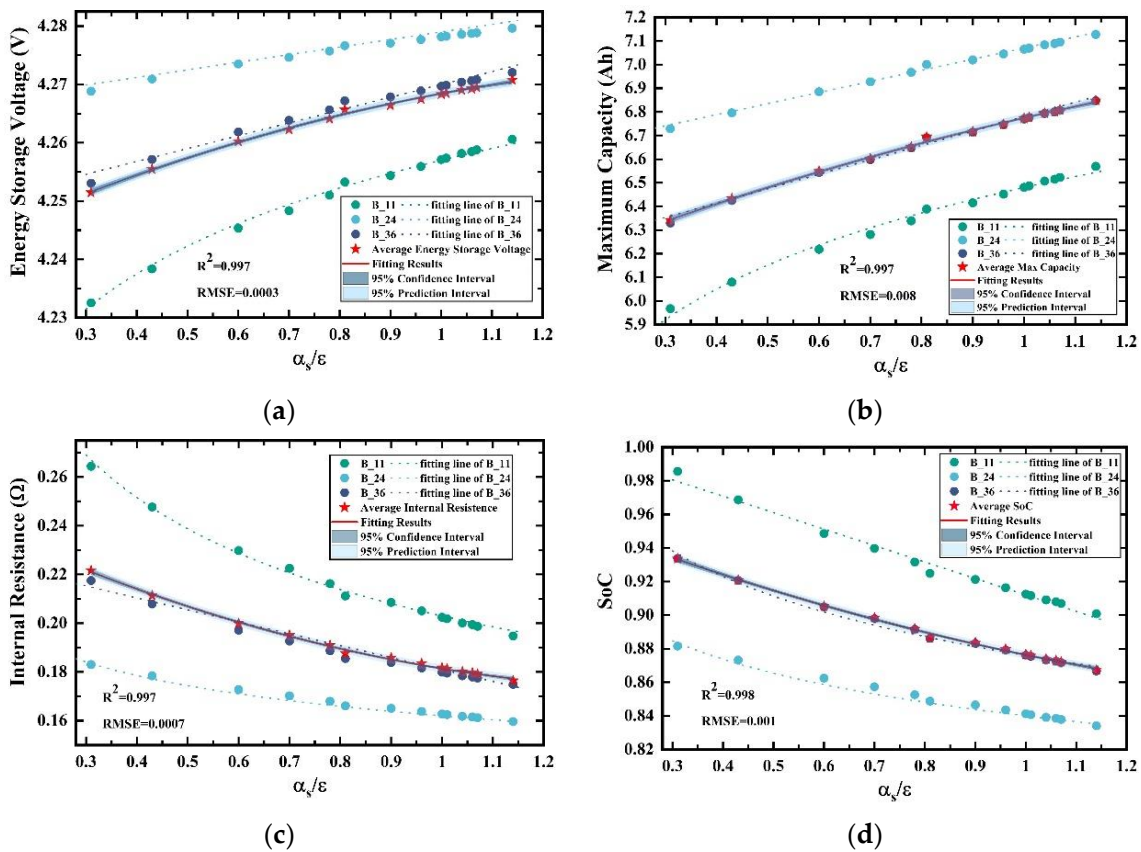


Figure 12. The electric parameters changing with different thermal-insulation surface's coating: (a) energy storage voltage; (b) maximum capacity; (c) internal resistance; (d) SoC.

5. Conclusions

Thermal control is important for on-orbit satellites, and thermal control coatings have long been recognized as an effective method for passive thermal design. Temperatures in satellites are determined by the coatings' α/ε . However, α/ε 's comprehensive impacts on the satellite environment and the Li-ion battery pack in the power system are not clear. Limited data and statistical analyses of electric–thermal behavior affected by α/ε exist in recent literature. In this work, we fill this gap by conducting multiphysics models of space Li-ion battery power systems and a numerical analysis of electric–thermal behaviors. Additionally, a newly defined characteristic value—energy storage voltage—is introduced to show the energy state of the battery pack. The results from our analysis are:

- The trends in temperature and electric–thermal behavior change with α/ε are similar in the radiator surface and thermal insulation surface. Thermal control coatings are selected according to the functions of the surfaces.
- Average temperatures and the temperature differences in the battery pack increase with α/ε , while the fluctuation of a single cell's temperature declines.
- The energy storage state of the battery will be improved and the internal resistance and SoC would drop with the growth of α/ε . However, these optimizations come at the cost of higher temperatures.

Our research can provide support for the selection of coating in future space engineering. A limitation of this study is that the selection of coatings does not mention the latest achievements. In forthcoming work, these limitations will be overcome, the electric–thermal behavior regulation will be extended to battery aging studies.

Author Contributions: Each author has made substantial contributions to this work. Their specific contributions are: Methodology, J.X. and Y.S.; Investigation, L.Y.; Writing, J.X.; Project Administration, Y.-Z.L.; Supervision, Y.-Z.L. All authors have read and agreed to the published version of the manuscript.

Funding: This research is financially supported by Beijing Institute of Spacecraft System Engineering under grant KH526-065-01.

Institutional Review Board Statement: Not applicable.

Informed Consent Statement: Not applicable.

Data Availability Statement: All data and models used in this study are in the published article.

Conflicts of Interest: The authors declare that they have no known competing financial interests or personal relationships that could have appeared to influence the work reported in this paper.

Notation

Nomenclature

A	Area [m^2]
S	Solar constant
P	Power [W]
q	Input energy density [W/m^2]
U	Voltage of the battery pack [V]
I	Current of the battery pack [A]
C_E	Capacitance [F]
C_H	Heat capacity [J/K]
u	Voltage of a single battery cell [V]
i	Current of a single battery cell [A]
R	Resistance [Ω]
a	Charging coefficient
b	Discharging coefficient
E	Electric energy [J]
SoC	State of capacity
K	Heat transfer coefficient [$\text{W}/(\text{m}^2 \cdot \text{K})$]
Q	Thermal energy [J]

Greek symbol

α	Absorbptivity
ε	Emissivity
σ	Stefan-Boltzmann constant
η	Efficiency
β	Temperature correction coefficient of PV's voltage
τ	Time [s]
ζ	Capacity [Ah]

Subscript

c	Satellite cabin environment
s	Thermal-insulation-surface
r	Radiator surface
sa	Solar array
B	Battery pack
b	Single battery cell
L	Payloads
d	Energy storage
un	Unused
max	Maximum
in	Input
out	Output
c	Satellite
0	Initial value
or	Ohm resistance
pr	Polarization resistance
dr	Self-discharge resistance
cs	Cabin environment with thermal-insulation-surface
cr	Cabin environment with radiator surface
sr	Thermal-insulation-surface with radiator surface
ij	Row and column numbers
bc	Battery cell with cabin environment
bs	Battery cell with thermal-insulation-surface
br	Battery cell with radiator surface
bx	Battery pack's environment
T	Values at temperature T K

Appendix A

The internal resistance of a battery cell is affected by its temperature and SoC. However, there has no expression to show the relationship between these variables. Data fitting is adopted, and the data from Figure 3.12 in [27] are represented in Table A1. The fitting equation is written as Equation (A1):

$$R_{in} = (R_a + R_t) \times B_0 \times T_b^{B_1} \times SoC^{B_2} \quad (\text{A1})$$

Table A1. Internal resistance vs. temperature at various SoCs.

T_b (K)	SoC	R_{in} (Ω)	T_b (K)	SoC	R_{in} (Ω)
258	0.05	6.1	283	0.05	2.5
	0.3	5.8		0.3	2.1
	0.5	5.5		0.5	2
	1	5.1		1	2
263	0.05	5.05	288	0.05	2.1
	0.3	4.8		0.3	1.95
	0.5	4.6		0.5	1.8
	1	4.2		1	1.8
268	0.05	4.1	293	0.05	2
	0.3	3.9		0.3	1.85
	0.5	3.85		0.5	1.5
	1	3.5		1	1.5
273	0.05	3.55	298	0.05	1.9
	0.3	3.1		0.3	1.8
	0.5	3		0.5	1.3
	1	2.95		1	1.3
278	0.05	3		0.05	
	0.3	2.65		0.3	
	0.5	2.25		0.5	
	1	2.2		1	

Equation (A2) takes the ln of both sides of this equation:

$$\ln R_{in} = \ln[(R_a + R_t) \times B_0] + B_1 \times \ln T_b + B_2 \times \ln \text{SoC} \quad (\text{A2})$$

The parameters $B_0 - B_1$ were obtained by data fitting: $B_0 = e^{49.48}$, $B_1 = -8.68$, $B_2 = -0.09$ ($R^2 = 0.948$).

The expression of capacity, temperature and charging rate is written as Equation (A3):

$$\zeta_T = \zeta_0 \times A_0 \times T_b^{A_1} \times I_t^{A_2} \quad (\text{A3})$$

Fitting data shown in Table A2 are obtained from Figure 2 in [28]. Take the ln of both sides of this equation, and the parameters are calculated: $A_0 = 1.86 \times 10^{-4}$, $A_1 = 1.497$, $A_2 = -0.51$ ($R^2 = 0.61$).

Table A2. Capacity vs. temperature at various charging rates.

I_t	T_b (K)	ζ_T (Ah)	I_t	T_b (K)	ζ_T (Ah)
0.25	308	2.2	1	308	1.98
	298	2.05		298	1.95
	278	1.81		278	1.72
	268	1.65		268	1.56
	258	1.49		258	1.38
0.5	308	2	1.5	308	1.95
	298	1.98		298	1.91
	278	1.78		278	1.72
	268	1.6		268	1.58
	258	1.43		258	1.39
0.75	308	1.99	2	308	1.94
	298	1.96		298	1.91
	278	1.76		278	1.73
	268	1.59		268	1.61
	258	1.4		258	1.41

Appendix B

The fitting results with radiator surfaces' α_r/ε are provided in Tables A3–A6 and the fitting results with thermal insulation surfaces' α_s/ε are provided in Tables A7–A10.

Table A3. The fitting polynomial and parameters of energy storage voltage changing with α_r/ε .

Fitting polynomial 1	$U_{es_i} = a_i + b_i \times \frac{\alpha_r}{\varepsilon} + d_i \times \frac{\alpha_r^2}{\varepsilon} + f_i \times \frac{\alpha_r^3}{\varepsilon} + g_i \times \frac{\alpha_r^4}{\varepsilon}$				
Parameters	a_i	b_i	d_i	f_i	g_i
Whole pack	4.27	−0.16	0.78	−1.12	0.51
Fitting polynomial 2	$U_{es_i} = a_i \times \frac{\alpha_r b_1}{\varepsilon}$				
Parameters	a_i	b_i			
B_11	4.28	0.003			
B_24	4.29	0.0027			
B_36	4.286	0.0028			
Error analysis	Whole pack	B_11	B_24	B_36	
R-square	0.961	0.895	0.89	0.894	
RMSE	0.002	0.003	0.002	0.0025	

Table A4. The fitting polynomial and parameters of maximum capacity changing with α_r/ε .

Fitting polynomial 1	$C_{max_i} = a_i + b_i \times \frac{\alpha_r}{\varepsilon} + d_i \times \frac{\alpha_r^2}{\varepsilon} + f_i \times \frac{\alpha_r^3}{\varepsilon} + g_i \times \frac{\alpha_r^4}{\varepsilon}$				
Parameters	a_i	b_i	d_i	f_i	g_i
Whole pack	6.97	−5.83	26.71	−37.49	17.05
Fitting polynomial 2	$C_{max_i} = a_i \times \frac{\alpha_r b_1}{\varepsilon}$				
Parameters	a_i	b_i			
B_11	7.11	0.055			
B_24	7.57	0.063			
B_36	7.39	0.058			
Error analysis	Whole pack	B_11	B_24	B_36	
R-square	0.951	0.9	0.89	0.895	
RMSE	0.058	0.077	0.094	0.085	

Table A5. The fitting polynomial and parameters of internal resistance changing with α_r/ε .

Fitting polynomial 1	$\Omega_i = a_i + b_i \times \frac{\alpha_r}{\varepsilon} + d_i \times \frac{\alpha_r^2}{\varepsilon} + f_i \times \frac{\alpha_r^3}{\varepsilon} + g_i \times \frac{\alpha_r^4}{\varepsilon}$				
Parameters	a_i	b_i	d_i	f_i	g_i
Whole pack	0.18	0.31	−1.51	2.17	−1.00
B_11	0.19	0.34	−1.66	2.39	−1.1
B_24	0.17	0.28	−1.4	2.02	−0.93
B_36	0.17	0.3	−1.46	2.1	−0.97
Error analysis	Whole pack	B_11	B_24	B_36	
R-square	0.962	0.962	0.962	0.962	
RMSE	0.003	0.003	0.003	0.003	

Table A6. The fitting polynomial and parameters of SoC changing with α_r/ε .

Fitting polynomial 1	$SoC_i = a_i + b_i \times \frac{\alpha_r}{\varepsilon_r} + d_i \times \frac{\alpha_r^2}{\varepsilon_r} + f_i \times \frac{\alpha_r^3}{\varepsilon_r} + g_i \times \frac{\alpha_r^4}{\varepsilon_r}$				
Parameters	a_i	b_i	d_i	f_i	g_i
Whole pack	0.86	0.67	-3.11	4.39	-2.01
Fitting polynomial 2	$SoC_i = a_i \times \left(\frac{\alpha_r}{\varepsilon_r}\right)^{b_1} + d_i$				
Parameters	a_i	b_i	d_i		
B_11	-0.46	0.11	1.29		
B_24	-0.49	0.12	1.28		
B_36	-0.47	0.11	1.28		
Error analysis	Whole pack	B_11	B_24	B_36	
R-square	0.955	0.89	0.89	0.89	
RMSE	0.007	0.01	0.01	0.01	

Table A7. The fitting polynomial and parameters of energy storage voltage changing with α_s/ε .

Fitting polynomial 1	$U_{es_i} = a_i + b_i \times \frac{\alpha_r}{\varepsilon_r} + d_i \times \frac{\alpha_r^2}{\varepsilon_r}$			
Parameters	a_i	b_i	d_i	
Whole pack	4.24	0.04	-0.01	
Fitting polynomial 2	$U_{es_i} = a_i \times \left(\frac{\alpha_r}{\varepsilon_r}\right)^{b_1}$			
Parameters	a_i	b_i		
B_11	4.257	0.005		
Fitting polynomial 3	$U_{es_i} = a_i \times \frac{\alpha_r}{\varepsilon_r} + b_i$			
Parameters	a_i	b_i		
B_24	0.013	4.266		
B_36	0.022	4.248		
Error analysis	Whole pack	B_11	B_24	B_36
R-square	0.997	0.995	0.987	0.979
RMSE	0.0003	0.0006	0.0004	0.0008

Table A8. The fitting polynomial and parameters of maximum capacity changing with α_s/ε .

Fitting polynomial 1	$C_{max_i} = a_i + b_i \times \frac{\alpha_r}{\varepsilon_r} + d_i \times \frac{\alpha_r^2}{\varepsilon_r}$			
Parameters	a_i	b_i	d_i	
Whole pack	6.1	0.86	-0.18	
Fitting polynomial 2	$C_{max_i} = a_i \times \left(\frac{\alpha_r}{\varepsilon_r}\right)^{b_1}$			
Parameters	a_i	b_i		
B_11	6.48	0.075		
Fitting polynomial 3	$C_{max_i} = a_i \times \frac{\alpha_r}{\varepsilon_r} + b_i$			
Parameters	a_i	b_i		
B_24	0.47	6.6		
B_36	0.61	6.17		
Error analysis	Whole pack	B_11	B_24	B_36
R-square	0.997	0.99	0.995	0.992
RMSE	0.0008	0.018	0.009	0.014

Table A9. The fitting polynomial and parameters of internal resistance changing with α_s/ε .

Fitting polynomial 1		$\Omega_i = a_i + b_i \times \frac{a_r}{\varepsilon_r} + d_i \times \frac{a_r^2}{\varepsilon_r}$		
Parameters	a_i	b_i	d_i	
Whole pack	0.25	−0.1	0.03	
Fitting polynomial 2		$\Omega_i = a_i \times \left(\frac{a_r}{\varepsilon_r}\right)^{b_1}$		
Parameters	a_i	b_i		
B_11	0.203	−0.234		
B_24	0.162	−0.106		
Fitting polynomial 3		$\Omega_i = a_i \times \frac{a_r}{\varepsilon_r} + b_i$		
Parameters	a_i	b_i		
B_36	−0.049	0.23		
Error analysis	Whole pack	B_11	B_24	B_36
R-square	0.997	0.995	0.99	0.975
RMSE	0.0007	0.001	0.0007	0.002

Table A10. The fitting polynomial and parameters of SoC changing with α_s/ε .

Fitting polynomial 1		$SoC_i = a_i + b_i \times \frac{a_r}{\varepsilon_r} + d_i \times \frac{a_r^2}{\varepsilon_r}$		
Parameters	a_i	b_i	d_i	
Whole pack	0.97	−0.12	0.03	
Fitting polynomial 2		$SoC_i = a_i \times \frac{a_r}{\varepsilon_r} + b_i$		
Parameters	a_i	b_i		
B_11	−0.098	1.01		
Fitting polynomial 3		$U_{es_i} = a_i \times \left(\frac{a_r}{\varepsilon_r}\right)^{b_1}$		
Parameters	a_i	b_i		
B_24	0.84	−0.043		
B_36	0.876	−0.057		
Error analysis	Whole pack	B_11	B_24	B_36
R-square	0.998	0.987	0.983	0.99
RMSE	0.001	0.003	0.002	0.002

References

1. Starner, K.E.; Stark, R.L. Effects of roughness on rear-surface mirror satellite coatings. *J. Spacecr. Rocket.* **1968**, *5*, 125–127. [\[CrossRef\]](#)
2. Putz, B.; Wurster, S.; Edwards, T.; Völker, B.; Milassin, G.; Többens, D.; Semprimoschnig, C.; Cordill, M. Mechanical and optical degradation of flexible optical solar reflectors during simulated low earth orbit thermal cycling. *Acta Astronaut.* **2020**, *175*, 277–289. [\[CrossRef\]](#)
3. Peters, J. System Level Testing of the Passive Thermal Control System for Space Station Freedom. In Proceedings of the 23rd International Conference on Environmental Systems, Colorado Springs, Colorado, 12–15 July 1993. [\[CrossRef\]](#)
4. Foster, J.A.; Aglietti, G.S. Strategies for Thermal Control of a Multifunctional Power Structure Solar Array. *J. Aerosp. Eng.* **2012**, *25*, 454–462. [\[CrossRef\]](#)
5. Swanson, T.D.; Birur, G.C. NASA thermal control technologies for robotic spacecraft. *Appl. Therm. Eng.* **2003**, *23*, 1055–1065. [\[CrossRef\]](#)
6. Haddad, E.; Kruzelecky, R.V.; Hendaoui, A.; Chaker, M.; Jamroz, W. Large Tuneability IR Emittance Thermal Control Coating for Space Applications. In Proceedings of the 43rd International Conference on Environmental Systems, Vail, CO, USA, 14–18 July 2013. [\[CrossRef\]](#)
7. Taylor, S.; Boman, N.; Chao, J.; Wang, L. Cryothermal vacuum measurement of thermochromic variable-emittance coatings with heating/cooling hysteresis for spacecraft thermal management. *Appl. Therm. Eng.* **2021**, *199*, 117561. [\[CrossRef\]](#)

8. Mandal, J.; Du, S.; Dontigny, M.; Zaghbi, K.; Yu, N.; Yang, Y. Li₄Ti₅O₁₂: A Visible-to-Infrared Broadband Electrochromic Material for Optical and Thermal Management. *Appl. Phys. Lett.* **2019**, *115*, 073902. [[CrossRef](#)]
9. Bertagne, C.L.; Cognata, T.J.; Sheth, R.B.; Dinsmore, C.E.; Hartl, D.J. Testing and analysis of a morphing radiator concept for thermal control of crewed space vehicles. *Appl. Therm. Eng.* **2017**, *124*, 986–1002. [[CrossRef](#)]
10. Johnson, J.; Cerbus, C.; Haines, A.; Kenny, M. Review of Improved Thermal Control Coating Development for NASA's SEE Program. In Proceedings of the 43rd AIAA Aerospace Sciences Meeting and Exhibit, Reno, Nevada, 10–13 January 2013. [[CrossRef](#)]
11. Fartash, A.H.; Poursaeidi, E. Thermal analysis of thermal barrier coating systems under transient and time harmonic thermal loads. *Appl. Therm. Eng.* **2022**, *208*, 118225. [[CrossRef](#)]
12. Athirah, N.; Afendi, M.; Hafizan, K.; Amin, N.; Majid, M.A. Stress and Thermal Analysis of CubeSat Structure. *Appl. Mech. Mater.* **2014**, *554*, 426–430. [[CrossRef](#)]
13. Corpino, S.; Caldera, M.; Nichele, F.; Masoero, M.; Viola, N. Thermal design and analysis of a nanosatellite in low earth orbit. *Acta Astronaut.* **2015**, *115*, 247–261. [[CrossRef](#)]
14. Reyes, L.A.; Cabriales-Gómez, R.; Chávez, C.E.; Bermúdez-Reyes, B. Thermal modeling of CIIASat nanosatellite: A tool for thermal barrier coating selection. *Appl. Therm. Eng.* **2020**, *166*, 114651. [[CrossRef](#)]
15. Wang, S.; Li, Y.; Li, Y. A forced gas cooling circle packaging with liquid cooling plate for the thermal management of li-ion batteries under space environment. *Appl. Therm. Eng.* **2017**, *123*, 929–939. [[CrossRef](#)]
16. Xu, H.-J.; Wang, J.-X.; Li, Y.-Z.; Bi, Y.-J.; Gao, L.-J. A Thermoelectric-Heat-Pump Employed Active Control Strategy for the Dynamic Cooling Ability Distribution of Liquid Cooling System for the Space Station's Main Power-Cell-Arrays. *Entropy* **2019**, *21*, 578. [[CrossRef](#)] [[PubMed](#)]
17. Bonkile, M.P.; Ramadesigan, V. Physics-based models in PV-battery hybrid power systems: Thermal management and degradation analysis. *J. Energy Storage* **2020**, *31*, 101458. [[CrossRef](#)]
18. Ma, S.; Jiang, M.; Tao, P.; Song, C.; Wu, J. Temperature effect and thermal impact in lithium-ion batteries: A review. *Prog. Nat. Sci. Mater. Int.* **2018**, *28*, 653–666. [[CrossRef](#)]
19. Luo, M.; Song, J.; Ling, Z.; Zhang, Z.; Fang, X. Phase change material coat for battery thermal management with integrated rapid heating and cooling functions from $-40\text{ }^{\circ}\text{C}$ to $50\text{ }^{\circ}\text{C}$. *Mater. Today Energy* **2021**, *20*, 100652. [[CrossRef](#)]
20. Feng, X.; Ouyang, M.; Liu, X.; Lu, L.; Fang, X. Thermal runaway mechanism of lithium ion battery for electric vehicles: A review. *Mater. Today Energy* **2018**, *10*, 246–267. [[CrossRef](#)]
21. Thomas, P.B.; Margot, L.W. Spacecraft Li-Ion Battery Power System State-of-Practice: A Critical Review. In Proceedings of the 2018 International Energy Conversion Engineering Conference, Cincinnati, OH, USA, 9–11 July 2018. [[CrossRef](#)]
22. Schoen, A.; Powers, A.R.; Arastu, A.; Canter, S.; Hall, J. High Performance Lithium Ion Battery Systems Development for Long Life Geostationary Satellites. In Proceedings of the 3rd International Energy Conversion Engineering Conference, San Francisco, CA, USA, 15–18 August 2005.
23. Bazarbayev, R.; Yakubov, K.; Kurbanov, D.; Allaniyazov, A.; Balakumar, S.; Kamalov, A.; Janabergenova, G.; Wei, Q.; Qian, H.; Polvonnazirov, I.; et al. Performance of crystalline Si solar cells and module on temperature and illumination intensity. *Mater. Today: Proc.* **2022**, *64*, 1661–1665. [[CrossRef](#)]
24. Cotfas, D.T.; Cotfas, P.A.; Machidon, O.M. Study of Temperature Coefficients for Parameters of Photovoltaic Cells. *Int. J. Photoenergy* **2018**, *2018*, 1–12. [[CrossRef](#)]
25. Bonnici, M.; Mollicone, P.; Fenech, M.; Azzopardi, M.A. Analytical and numerical models for thermal related design of a new pico-satellite. *Appl. Therm. Eng.* **2019**, *159*, 113908. [[CrossRef](#)]
26. Shrestha, S.; Del Pino, C.B.; Malayoglu, U. Inorganic White Thermal-Control Coatings for Extreme Space Environments. *J. Spacecr. Rocket.* **2016**, *53*, 1061–1067. [[CrossRef](#)]
27. Gong, X. Modeling of Lithium-ion Battery Considering Temperature and Aging Uncertainties. Ph.D. Thesis, University of Michigan Dearborn, Dearborn, MI, USA, 2016; p. 53.
28. Li, L.; Xie, Y.; Cao, L.; Huang, K. Analysis of different cathode materials of lithium-ion battery capacity characteristics. *Chin. J. Power Sources* **2017**, *41*, 1677–1680.

Disclaimer/Publisher's Note: The statements, opinions and data contained in all publications are solely those of the individual author(s) and contributor(s) and not of MDPI and/or the editor(s). MDPI and/or the editor(s) disclaim responsibility for any injury to people or property resulting from any ideas, methods, instructions or products referred to in the content.